Rotating particle pair produces hot complex plasma crystals

Calvin Carmichael ®,* Jorge Martinez Ortiz, Parker Adamson ®, Lorin Matthews ®, and Truell Hyde ®
CASPER (Center for Astrophysics, Space Physics, and Engineering Research), Baylor University, Waco, Texas 76798, USA

Rotating quasipaired particles (torsions) are observed within a two-dimensional monolayer crystal suspended in an argon complex plasma for discharge powers of 1–10 W and pressures of 135–155 mTorr. The inclusion of a torsion in a crystal lattice fundamentally changes the overall lattice state to a "hot crystal." A torsion increases the particle motion and kinetic energy of other particles in the crystal, with the strongest effects on neighboring particles. The apparent effective range is to the third nearest neighbor, with the kinetic energy in the first three shells of particles increasing by at least 200% over baseline values for the crystal. However, the variance of the motion of all particles in the crystal increases by more than two times over the average background kinetic fluctuations for the whole crystal. The formation of a torsion perturbs the structure and symmetry of a plasma crystal. A single torsion causes the average interparticle spacing to increase by 11% compared to the same crystal without a torsion. Particles in the first two shells surrounding a torsion also display reduced hexagonal symmetry. The combination of the perturbed lattice structure and the larger range of motion for the microparticles contribute to a higher-energy-state crystal when torsions are present.

I. INTRODUCTION

Complex plasmas consist of ionized gas with embedded nanometer to micron-sized particles. The microparticles typically attain a net negative electric charge by collecting electrons from the plasma [1]. The relative strength of particle-particle interactions compared to particle-neutral gas momentum exchange determines the properties exhibited by a system, such as particle dynamics and phase transitions [2].

A common method for investigating complex plasma phenomena is to use a capacitively coupled plasma created between charged and grounded electrodes at low pressures. The charged microparticles levitate in the sheath above the negatively charged lower electrode due to a balance between the electrostatic and gravitational forces [3]. The system parameters can be adjusted so that the charged particles experience a strong electrostatic coupling between the particles, which occurs when the particle interaction energy is greater than the thermal energy of the microparticles. With sufficient vertical and horizontal confinement of the system, microparticles can form a hexagonally symmetric monolayer structure, known as a plasma crystal [4–7]. Plasma crystals offer unique insight into ordinary solids and phase transitions. Plasma crystals provide the advantage of direct examination of the particle motion governing the fundamental physics involved in wave mechanics, melting dynamics, phase transitions, and Mach Cone formation [8–13].

An electric field is required to levitate the negatively charged particles, and an ion wakefield is created downstream of each particle by ions flowing toward the negatively charged lower electrode [14–18]. The ion wake results in apparent nonreciprocal forces between neighboring microparticles levitating at different heights as negative particles are attracted to the positive wake of neighboring upstream particles [19].

Previous examinations of particles located below the monolayer plane of a plasma crystal have been reported in Ref. [20] where a free particle moving below the lattice causes structural deviations as well as excess heating and melting in the lattice. The spontaneous motion and heating observed in the lattice are thought to be caused by the ion wakefield. Similar observations were recorded in Ref. [21] where a particle trapped above the monolayer caused attraction-based mach cones to form in the lattice when moving across the monolayer at supersonic speeds. Experiments on multilayer crystals confirming the presence of the ion wakefield and its attraction effects on neighboring dust grains are reported in Ref. [22], with the effect on the structure and arrangement of the crystal from the electric field and ion wakefield reported in Ref. [23].

This paper examines a feature recently identified in monolayer plasma crystals. Torsions are quasipaired particles levitating above and below the plane of the microparticle monolayer which circle around a common axis [24–26]. These disruptions caused by particles above or below the monolayer moving across the lattice differ from torsion systems, where the particles above and below the monolayer present repetitive circular or elliptical motion about a fixed point in the crystal lattice. The pairing of the torsion particles is due to the nonreciprocal nature of the ion wakefield [19]. The microparticle levitating above the crystal plane leads the rotational motion (leader), with the satellite particle attracted to the leader's ion wake. The motion of the torsion pair perturbs the surrounding particles in the crystal.

The torsion formation process most often occurs when a set of neighboring particles are forced out of the plane of

---

*Contact author: Calvin_Carmichael1@baylor.edu

the monolayer by a sharp decrease in power [24–26]. The change in power (and thus changes in the applied vertical confinement) is similar to the mechanism that causes a vertical chain of particles to transition from a one-dimensional (1D) chain to a two-dimensional zigzag structure [27] where the vertical alignment is thought to be aided by the ion wake. A difference between the zigzag structure and torsions is that although a one-dimensional chain transforms into a two-dimensional zigzag pattern through an increase in vertical confinement (compression), a two-dimensional crystal can have a three-dimensional torsion feature form from weakened vertical confinement (relaxation). Another difference is that a torsion is a dynamic structure, in contrast to the stable zigzag pattern.

The microparticles in the crystal oscillate around an equilibrium position. The system kinetic energy and the crystal's structure factors can parametrize a plasma crystal's characteristics. The kinetic energy is measured from individual microparticle motion [4–6,10]. The structure factors are based on the equilibrium positions of the microparticles. Local variations in kinetic energy play a significant role in the structure of a complex plasma system, namely, the interparticle spacing (Δ) and the hexagonal symmetry (Ψ_6) of surrounding cells.

Torsions are known to increase the local kinetic energy of a system [24–26]; however, torsion systems have not been examined in depth. Given that torsions are still a newly discovered characteristic of plasma crystals, their structural effects in plasma crystals are largely unknown. We compare the motion of the particles in a crystal with a torsion present to the background motion of particles in crystals without torsions for similar plasma conditions. In this work, we examine the structural perturbations caused by a single torsion in a crystal lattice, as defined by the interparticle spacing, the hexagonal symmetry of the system, and the increase in kinetic energy. The structure of a crystal is fundamental to physical processes in the system, impacting the propagation of waves, interparticle forces, and particle dynamics. Thus, any change in the crystal structure due to a torsion alters the effective forces. Analysis of the effects of a single torsion on the plasma crystal structure is a necessary component of understanding the effect of multiple torsions, which may be considered analogous to the vortical motion seen in two-dimensional melting. These combined effects increase system energy, resulting in a state of a "hot crystal" as defined in Ref. [1].

II. EXPERIMENTAL SETUP AND PROCEDURE

The data for this project were collected in a modified Gaseous Electronics Conference Radio Frequency Reference Cell (Fig. 1) [28]. A flat, 10.08-cm diameter aluminum plate grooved with a circular, 1-mm deep, 2.54-cm diameter cutout was placed on the lower electrode to provide radial confinement for the particles. A power supply with a maximum output of 50 W was connected to the lower electrode. Particles were dispersed from a microparticle dropper (above the upper electrode) connected to the grounded walls of the chamber. Argon was introduced into the cell through annular slots near the base of the lower electrode column, designed to minimize the perturbation of particles due to indirect gas flow. For this
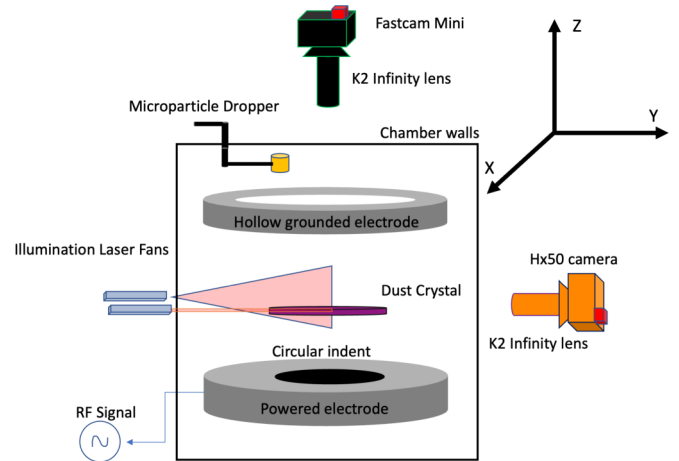

FIG. 1. Particles are levitated above the lower electrode and confined by a 2.54-cm-diameter cylindrical indentation in the lower electrode plate. Laser fans illuminate the layer in both the horizontal and vertical planes. The coordinate axis is shown with the *x* axis coming out of the page.

experiment, gas flow rates of 5–10 standard cubic centimeters per minute were employed for optimal crystal formation.

Plasma crystals are formed by dropping particles into an active plasma environment. The particles used in this experiment were monodisperse melamine-formaldehyde spheres with diameters of 8.89 ± 0.09 μm and a density of 1510 $\mathrm{kg m^{-3}}$. A monolayer system is formed by lowering the power, thus decreasing the discharge's vertical confinement, allowing excess particles to fall to the lower electrode. The power is then increased to the desired operating value. Microparticles were illuminated using Stingray 100- and 80-mW lasers aligned in vertical and horizontal directions. The horizontal laser fan was employed to vertically scan the resulting crystal and ensure uniformity of the monolayer. The vertically fanned laser illuminated a single row of particles along the crystal plane. Particles illuminated by the horizontal laser fan are tracked from the top using a Fastcam Mini UX50, and particles illuminated by the vertical laser fan are imaged from the side using a Sony XR50 camera equipped with infinity K2 lenses. The Fastcam Mini UX50 can operate at 500 frames per second (FPS), while the Sony XR50 can record up to 120 FPS.

Cameras are mounted on VEXTA/Valvex stepper-motor assemblies, enabling high-resolution precision scanning through the crystal plane. A view of the crystal can be seen from the top camera in Fig. 2. Figure 2 shows stacked frames of a crystal without a torsion and a crystal with a torsion. The motion of all particles in the crystal increases when a torsion is present [Fig. 2(b)], characterized as a hot crystal. The "hot crystal's" characteristics can be quantified by comparing the energy and motion of particles to those in a crystal without a torsion present.

Figure 3 shows several images recorded by the side camera. The vertical motion imposed by the torsion pair on neighboring particles is evident in these images and described more fully in Sec. III. The tracking data can be seen in the following Supplemental Material data [29].
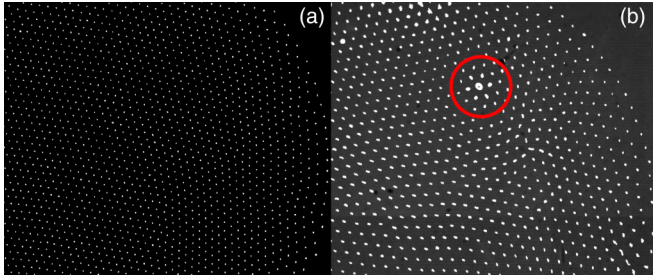
FIG. 2. The same crystal is shown for operating parameters of 155 mTorr and 5 W. Both photos are stacked images of 750 consecutive frames. The crystal in (a) has no torsion present, and the crystal in (b) has a torsion located inside the red circle.

Once the monolayer was sufficiently stable, the background motion of the particles in the crystal was recorded to determine the average horizontal (in-plane) and vertical (out-of-plane) motion due to kinetic fluctuations. In each crystal, a row of particles in the middle of the crystal was illuminated with vertical and horizontal laser fans, and the motion of the particles was tracked at each power and pressure.

After recording the background motion, a sharp decrease in applied power, $\Delta P_a = 0.25$–1 W, was used to initiate torsion formation. The power was not altered after the torsion formed. The monolayer was scanned again to ensure that the only particles outside of the monolayer were the torsion particles. This procedure was repeated for a range of gas pressures ($P = 135$–155 mTorr) and applied powers ($P_a = 2$–10 W). The parameter space identified for the formation of torsions, shown in Fig. 4, is consistent with the findings of previous
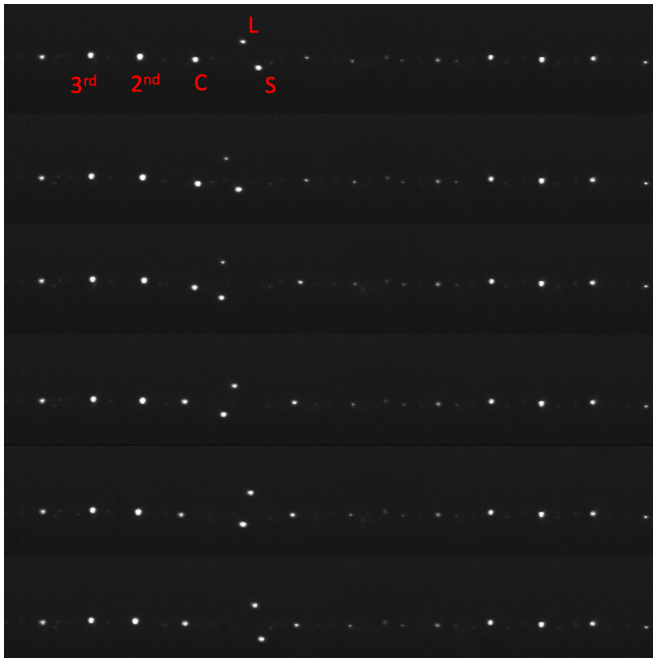

FIG. 3. Six consecutive frames from the side view camera are shown with particles illuminated by the vertical laser fan. The particles are labeled as follows: L (Leader), S (Satellite), C (Cage), 2nd (second shell), and 3rd (third shell). See Figs. 8 and 9 for a definition of the particle designations.
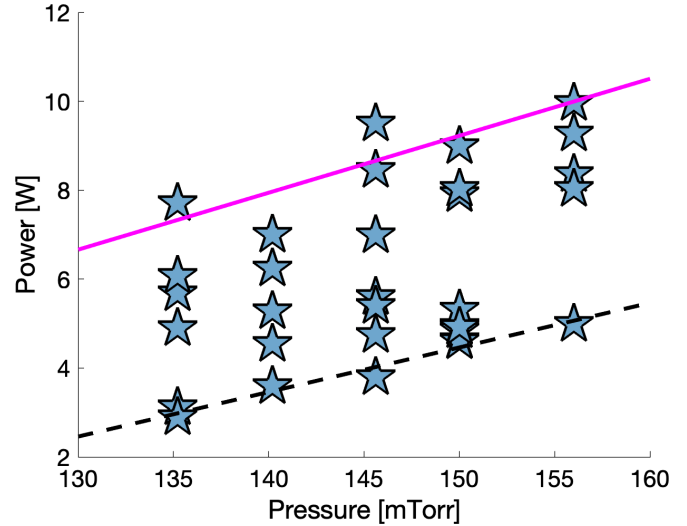

FIG. 4. Parameter space where torsions formed. The lines are linear fits to the highest (solid) and lowest (dashed) powers for which torsions were observed at a given pressure.

investigations [25,26]. The power necessary for the formation of a torsion grows linearly with the gas pressure. Assuming the indicated linear trends shown in Fig. 4, the lowest pressure at which a torsion should form is approximately 78 mTorr, in agreement with the results in Ref. [30].

After a sharp decrease in power, the top particle (leader) remains at nearly the same height. In contrast, the bottom particle (satellite) drops with the rest of the microparticles in the monolayer. During the transition, the leader particle moves into the space between the previous equilibrium positions of the leader and satellite particles in the crystal lattice, which bestows initial angular momentum to the leader particle. The satellite is attracted to the leader's wakefield and is forced down further than other particles in the crystal due to the repulsion of the leader. The satellite then follows the leader, attracted to the leader's wake, and the quasipair experiences a visible increase in angular momentum due to the repulsion of the surrounding charged particles.

III. RESULTS

A. Background motion without a torsion

Figures 5 and 6 show the average vertical and horizontal displacements of particles in stable monolayers without a torsion as a function of power and pressure. The measurements are normalized by their respective crystal's interparticle spacing (Δ) and can be found in Table I.

The average particle positions were measured using an intensity-weighted average over each illuminated pixel, yielding subpixel accuracy. The pixel resolution for the top camera is calculated to be 12.6 microns per pixel, and the side camera is 7.3 microns per pixel. The average displacement is defined as the distance a microparticle is displaced from its equilibrium position, averaged over time. Note that the range of vertical motion depends on the viewing angle. The vertically fanned laser only illuminates two of the cage particles in the fixed viewing plane of the side camera. Components of
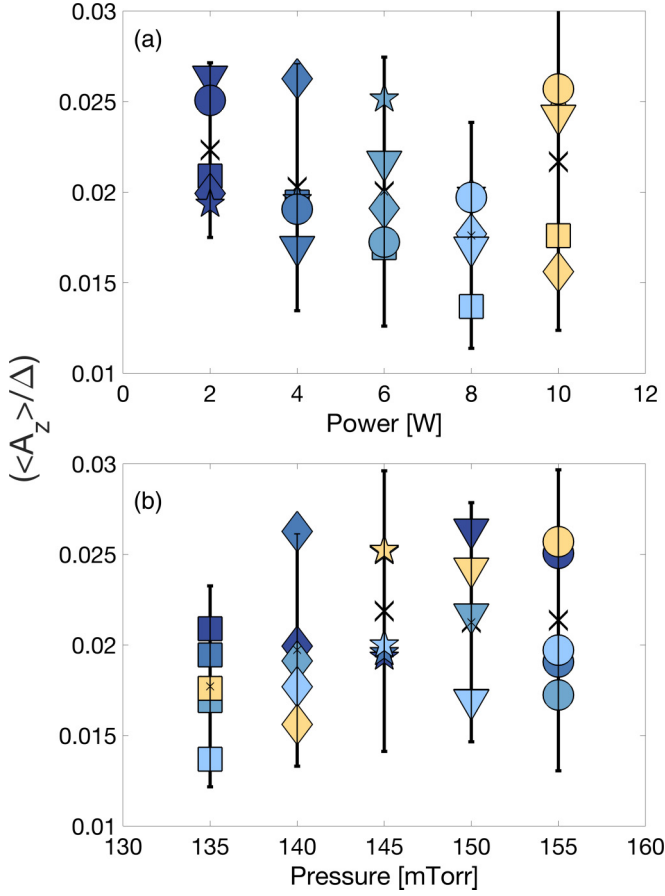
FIG. 5. The average vertical displacement for background particle motion as a function of (a) power and (b) pressure. The black X and the error bars denote the mean and standard deviation for all experiments at a given power (pressure), with the shaded symbols showing the average for each experiment at a specific pressure and power. All markers with the same color denote experiments at the same power while experiments at the same pressure have the same symbol shape (i.e., yellow circle corresponds to 10 W and 155 mTorr).

the motion perpendicular to the viewing direction may be lost. The variance of particle motion for $\langle A_x \rangle$ and $\langle A_z \rangle$ were calculated from the distribution of observed values. Results from each experiment are shown in Table I, which gives the operating parameters of the system being observed, the average displacement, $\langle A_x \rangle$ and $\langle A_z \rangle$, corresponding to in-plane horizontal motion and vertical displacement outside the monolayer, respectively, the background kinetic energy, and the average interparticle spacing Δ. The kinetic energy is the average of the kinetic energy of all particles in the crystal, $KE_b = \Sigma \frac{KE_P}{N}$, where N is the total particles in the crystal. The interparticle spacing was calculated using the first peak of the pair correlation function (PCF) for each crystal; an example of a PCF for a crystal with and without a torsion is shown in Fig. 7. The radial pair correlation function for particles in a two-dimensional plane, $G(r)$, is defined as

$$G(r) = \frac{1}{n_d N} \sum_{i \neq j}^{N} \frac{\delta(r - r_{ij})}{2\pi r \Delta r}, \quad (1)$$
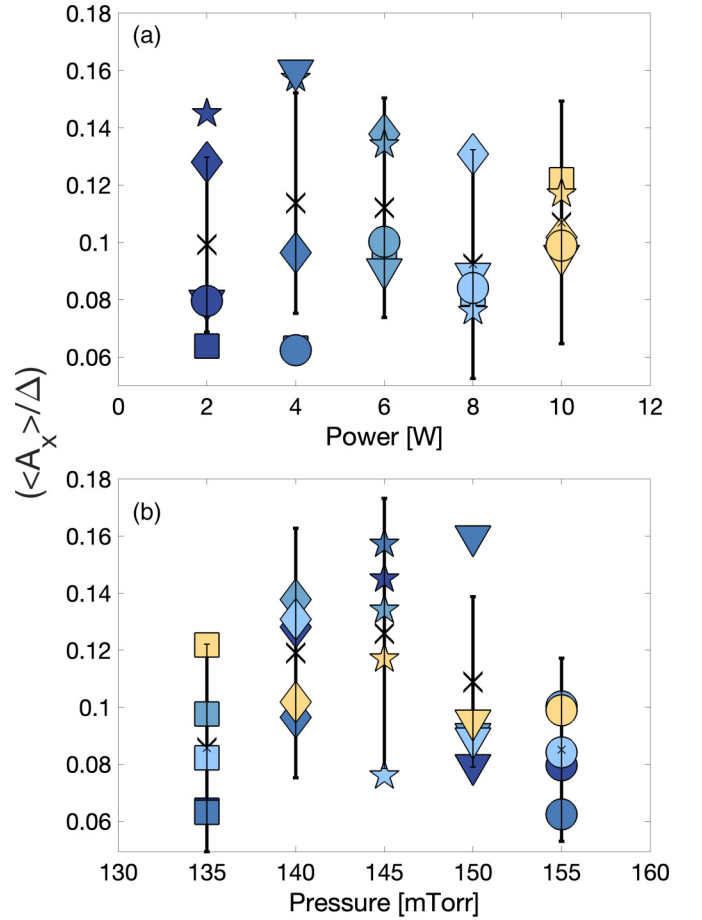

FIG. 6. Average horizontal displacement of background particle motion as a function of (a) power and (b) pressure. See Fig. 5 for a description of the symbols.

where n_d is the two-dimensional number density, N is the total number of particles, and r_{ij} is the distance between particles i and j. The normalization reflects the average number of particles expected to be found in an annular ring centered on particle i with radius r and width Δr.

Small measured values for $\langle A_z \rangle$, less than three percent of the average Δ, show that the monolayer is tightly constrained in the vertical direction when no torsions are present in the crystal. Figure 5 shows that the normalized background motion in the vertical direction remains relatively constant across the range of powers and pressures investigated and is essentially independent of the power and pressure. In contrast, motion in the horizontal direction (Fig. 6) is about 16% of the average interparticle spacing and slightly dependent on the pressure. In this case, there is an observed increase in the average displacement at 145 mTorr, almost irrespective of power, compared to other pressures. At lower pressures, the Debye length is longer, and particle motion is constrained due to longer interaction distances; conversely, at higher pressures, the Debye length shrinks, and a higher drag coefficient constrains the particle motion. We surmise that at 145 mTorr, the competing forces of the increasing drag and decreasing Debye length cause a maximum particle displacement; however, this change in plasma regime at this pressure warrants further investigation. The confinement is stronger in the vertical

TABLE I. Background kinetic motion for the powers and pressures used in the experiment. Rows in bold are best for comparison with Table II.

Power (W)	Pressure (mTorr)	$\langle A_x \rangle$ (μm)	$\langle A_z \rangle$ (μm)	KE_b (eV)	Δ (μm)
	135	20 ± 4.0	11 ± 2.2	0.16 ± 0.06	430 ± 7
	140	23 ± 5.6	8.0 ± 1.9	0.19 ± 0.09	431 ± 7
	145	26 ± 6.5	11 ± 2.2	0.22 ± 0.06	438 ± 7
	150	13 ± 3.2	11 ± 1.9	0.25 ± 900	299 ± 5
2	155	31 ± 6.2	8.7 ± 2.1	0.21 ± 0.09	392 ± 6
	135	28 ± 6.0	10 ± 2.2	0.26 ± 0.12	386 ± 6
	140	47 ± 9.3	9.7 ± 2.5	0.36 ± 0.16	387 ± 6
	145	33 ± 8.1	10 ± 2.4	0.47 ± 0.17	307 ± 5
	150	45 ± 8.9	7.9 ± 1.9	0.16 ± 0.09	445 ± 7
4	**155**	$\mathbf{24 \pm 4.6}$	$\mathbf{12 \pm 2.4}$	$\mathbf{0.38 \pm 0.16}$	$\mathbf{390 \pm 7}$
	135	32 ± 6.6	10 ± 2.2	0.25 ± 0.08	358 ± 6
	140	66 ± 11	6.0 ± 2.0	0.38 ± 0.12	389 ± 6
	145	50 ± 8.1	9.0 ± 1.5	0.51 ± 0.17	369 ± 6
	150	24 ± 4.7	7.2 ± 1.7	0.29 ± 0.13	339 ± 5
6	**155**	$\mathbf{30 \pm 5.8}$	$\mathbf{10 \pm 2.2}$	$\mathbf{0.22 \pm 0.12}$	$\mathbf{377 \pm 6}$
	135	26 ± 5.2	10 ± 1.9	0.19 ± 0.08	412 ± 7
	140	37 ± 7.3	7.7 ± 1.5	0.38 ± 0.17	372 ± 6
	145	33 ± 6.4	10 ± 1.6	0.30 ± 0.08	373 ± 6
	150	31 ± 6.1	11 ± 2.8	0.43 ± 0.18	372 ± 6
8	155	29 ± 5.6	7.0 ± 1.3	0.16 ± 0.06	375 ± 6
	135	25 ± 6.1	7.2 ± 1.8	0.23 ± 0.09	336 ± 5
	140	40 ± 7.9	4.8 ± 1.1	0.34 ± 0.13	380 ± 6
	145	18 ± 4.3	11 ± 2.8	0.39 ± 0.13	304 ± 5
	150	22 ± 5.4	10 ± 2.1	0.27 ± 0.10	353 ± 6
10	155	25 ± 4.9	7.5 ± 1.4	0.21 ± 0.06	286 ± 4

direction than the horizontal direction, and observed particle motion is nearly two to three times lower.

B. Motion imposed by a torsion

Torsion particles never form a stationary pair. Therefore, we define this action as a quasipair since the pairing is
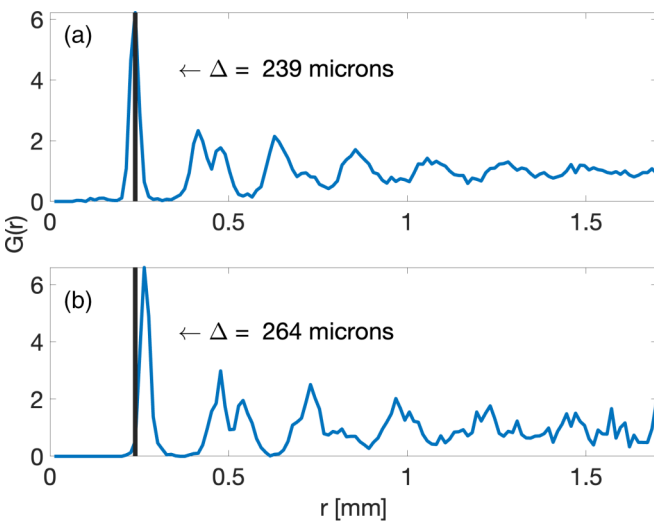

FIG. 7. Pair correlation function for a crystal (a) without a torsion present and (b) with a torsion present. The black line represents the interparticle spacing of a crystal without a torsion and visually demonstrates the shift in the first peak. Operating conditions 150 mTorr and 4.9 W.

dynamic. Such particle pairs are long-lived and can remain indefinitely in the same position in the crystal if conditions do not change. The vertical displacement of the satellite particle below the crystal layer is between 98 and 123 μm, as measured by the side camera, which is about 25% to 30% of the interparticle distance, making this effect a candidate to be driven by the lateral attraction to the leader's wakefield [19]. The diameter of torsion rotation is, on average, $0.53 \pm 0.15 \Delta$, where Δ is the average interparticle spacing. This value is somewhat dependent on the number density of microparticles in the lattice and cant be fully controlled in the experiment.

The kinetic motion of other particles, which arises due to the interaction of the torsion particles with the surrounding particles, is visible and quantifiable in all three dimensions. The vertical motion observed is primarily due to the attractive force of the leading particle's wakefield on the surrounding cage particles. In contrast, motion in the lattice plane is a response to the repulsion between the cage particles and the satellite particle, as illustrated in Figs. 7(a) and 7(b). The vertical and in-plane horizontal motion is given in Table II for a sample torsion (measured with the top and side camera) and is useful for comparison with background values in Table I. Slow motion video of torsion rotations shows that cage particles are attracted to the leader and then repelled by the trailing satellite (in this Supplemental Material data [29]).

These data and previous investigations indicate that the wake of the leader particle is "dragging" the satellite through rotations [26]. This motion continues indefinitely due to the continuous flow of ions from the bulk plasma unless power fluctuations flatten the torsion or pair other sets of

TABLE II. Torsion-imposed motion for particles surrounding a torsion. Operating parameters were 155 mTorr and 5 W.

Classification	$\langle A_x \rangle$(μm)	$\langle A_z \rangle$(μm)	KE (eV)	Δ (μm)
Cage	150 ± 54	60 ± 17	17.52 ± 1.78	314 ± 5
Second shell	57 ± 28	23 ± 10	2.83 ± 0.53	
Third shell	36 ± 18	13 ± 6.5	0.41 ± 0.15	
Fourth shell	30 ± 11	10 ± 6.0	0.21 ± 0.13	

particles. The perturbation to other particles is uniform in all directions.

Particles surrounding the torsion act as cage particles, confining the torsion pair in a tight circle around the equilibrium position that a single particle would occupy. The cage, 1st, and 2nd shell particles, indicated in Fig. 9, all exhibit a greater vertical and horizontal displacement than the kinetic background particle motion. As an example, the average displacement for different shells surrounding a torsion at a pressure of 155 mTorr and $P_a = 5$ W is provided in Table II. The particles in the third and fourth shells have an average displacement similar to microparticles in crystals without torsions. Still, the variance of the displacement is more than doubled compared with baseline data taken at similar power and pressure (Table I). While the average displacement is greater, the average velocity of the particles is relatively unaffected and is similar to that of background particles. The velocity and, therefore, the kinetic energy of the third and fourth shell particles is shown to be the same in Fig. 11. Figure 10 shows the average displacement in the horizontal direction for each particle shell around a torsion, normalized by the average interparticle distance of each crystal in which the torsions were observed. The magnitude of displacement is relatively constant across the powers studied, as shown by the trend lines. The magnitude of displacement is slightly positive across the pressures studied; the radial confinement decreases with increased pressure, promoting a larger range of motion for the particles to move.
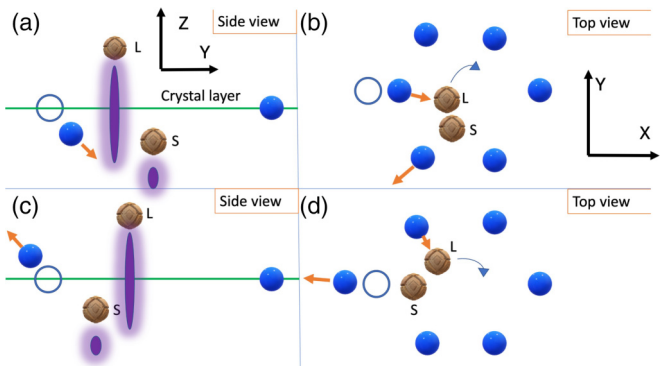

FIG. 8. Cage particle motion during torsion rotation. Filled blue circles denote cage particles with the purple area beneath the leader (L) and satellite (S) showing the respective wakefields. The open blue circle is the cage particle equilibrium position. Side view (a) and top view (b) show the attraction of the cage particles (blue) to the wake of the leader torsion particle (beige). Side view (c) and top view (d) shows a cage particle repelled by the satellite. The blue arrows in panels (b) and (d) denote the direction of rotation for the torsion particles.
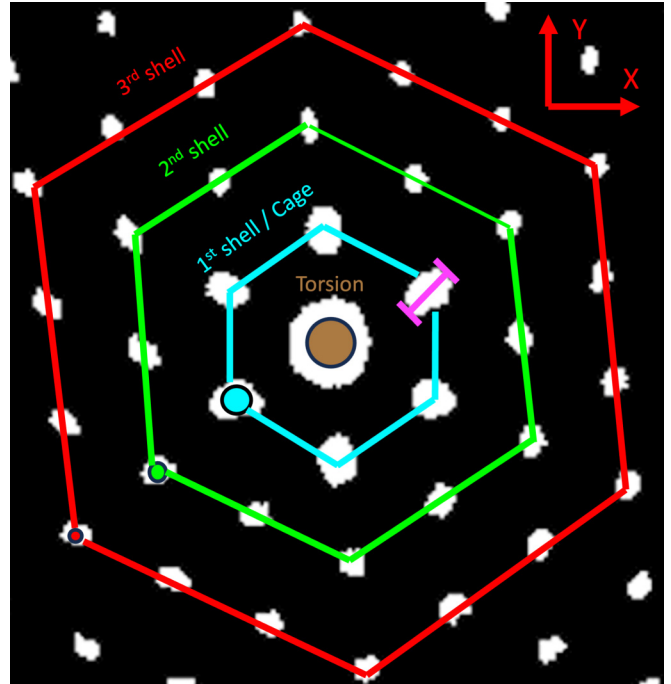

FIG. 9. Five hundred stacked frames of particle motion surrounding a torsion. The hexagons indicate the concentric shells surrounding a torsion. The circles have a radius equal to the average horizontal displacement, and the magenta line indicates the distance used to calculate the radial amplitude. The coordinate axes are given in the upper right quadrant of the figure and are used for Figs. 11, 14, and 16, with the z axis coming out of the page. A video of torsion rotation can be seen in the Supplemental Material [29].

Thus, we conclude that it is the presence of a torsion in a lattice that dictates the average displacement and motion of the surrounding crystal particles rather than the operating conditions. While the average displacement of the third and fourth shell particles tends to the background level of average displacement, the variance is 2.1–4.9 times the variance of the background kinetic motion, as seen by comparing values in Table I and Table II.

The increase in variance of particle position can be attributed to the asymmetrical displacement of the cage particles, where the majority of displacement is directed towards or away from the center of the torsion in a highly eccentric ellipse. The broken symmetry of the cage particle's motion increases the variance of a particle's position. The eccentricity of the cage particles' motion can be seen in a stacked image of all the frames for a single torsion in Fig. 9. As an example, the elliptical areas traced out by the motion of the cage particles shown in Fig. 9 have a variance in the average displacement 4.3% greater than a circle of equal area. The increase in variance was calculated by a Monte Carlo simulation of an ellipse overlapping a circle. As noted in Sec. III, although the third and fourth shell particles have the same average displacements as the background particles, the variance of the motion is increased. Given a similar average displacement for the furthest shells from the torsion, this increase in variance can be considered indicative of increasing the component of the motion directed away from the torsion.
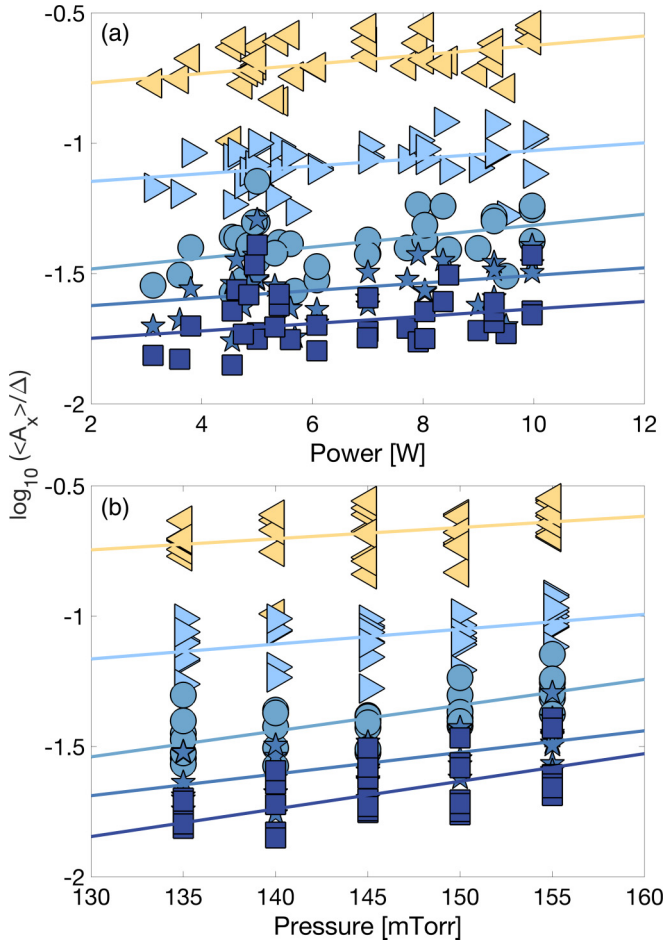
FIG. 10. The average horizontal displacement of particles as a function of (a) power and (b) pressure. From the top down, left-pointing triangles denote the data for torsion particles, right-pointing triangles for cage particles, circles for second-shell particles, stars for third-shell particles, and squares for background particles. Trend lines correspond to data points of the same shell.
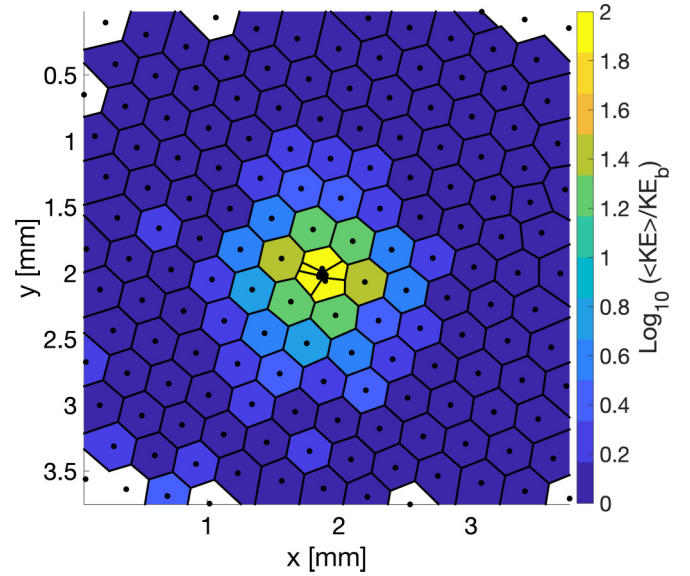

FIG. 11. Average kinetic energy. Each black dot is the average position of the microparticles calculated over 300 frames. The measurements are normalized by their respective background values denoted by KE_b, and each particle's kinetic energy is explicitly calculated with Eq. (2). Operating parameters were 145 mTorr and 4.75 W; displayed values do not represent the whole data parameter space, but best illustrate the torsion's effects on particles in neighboring shells.

IV. ANALYSIS

A. Kinetic energy

The kinetic energy of the particles in a complex plasma, KE_P, is defined by the motion of the microparticles [4–7,9,31,32]. The 2D kinetic energy can be defined by

$$KE_P = \tfrac{1}{2}m\langle v_x^2 + v_y^2\rangle \qquad (2)$$

where m is the mass of the particle, and $\langle v_x^2 + v_y^2\rangle$ is the mean-squared velocity of the microparticles in the crystal plane. The 2D kinetic energy was calculated from data from the top camera, which can view the entire crystal plane, as the vertical motion seen from the side camera only includes a few particles in the lattice. A crystal is defined as a quasi-2D structure due to the observed vertical fluctuation of the particles in the z direction. The 2D kinetic energy of the microparticles calculated from a few seconds of video data and the phase of a complex plasma can be confirmed, allowing the classification of the system as a liquid, solid, or gas. In complex plasma crystals, an increase in the local kinetic energy can give rise to "hot crystals" as defined in

Refs. [1,11,33–36] where the variance in motion of individual particles and the microparticle kinetic energy is higher, but doesn't lead to loss of order and melting in the lattice. Further increases in the kinetic energy or reductions in friction (neutral drag) for a hot crystal can lead to a phase transition to a liquid state where hexagonal order is lost, and particle kinetic energy can increase by a factor of 1000 [37].

The kinetic energy of the microparticles can be increased in multiple ways, including applying a thermal gradient to the plasma, laser perturbation, decreasing the vertical confinement, or changing the gas pressure. Decreasing the gas pressure reduces the neutral drag forces, leading to a greater average displacement of particles over time [38]. Similarly, decreasing the applied power to the lower electrode weakens the vertical confinement of the crystal, allowing particles to move more freely in the vertical plane and/or form paired structures [39]. In both cases, the increased particle motion leads to a higher average kinetic energy for the microparticles. In this experiment, no changes were made to the system other than adjusting power and pressure. Therefore, contributions to the change in microparticle kinetic energy from other mechanisms are assumed to be negligible.

The increase in kinetic energy observed in the shells surrounding a torsion is crucial to determining its interaction range with other particles. Here we define the torsion reach, which can be characterized as the extent of the excess energy propagation from a torsion. This energy transfer is considered truncated when the kinetic energy of an analyzed particle is less than 1.3 times the average background particle kinetic energy (i.e., within the range of background fluctuations). As shown in Fig. 11, the energy transfer from a single torsion does not affect the kinetic energy of the crystal lattice outside
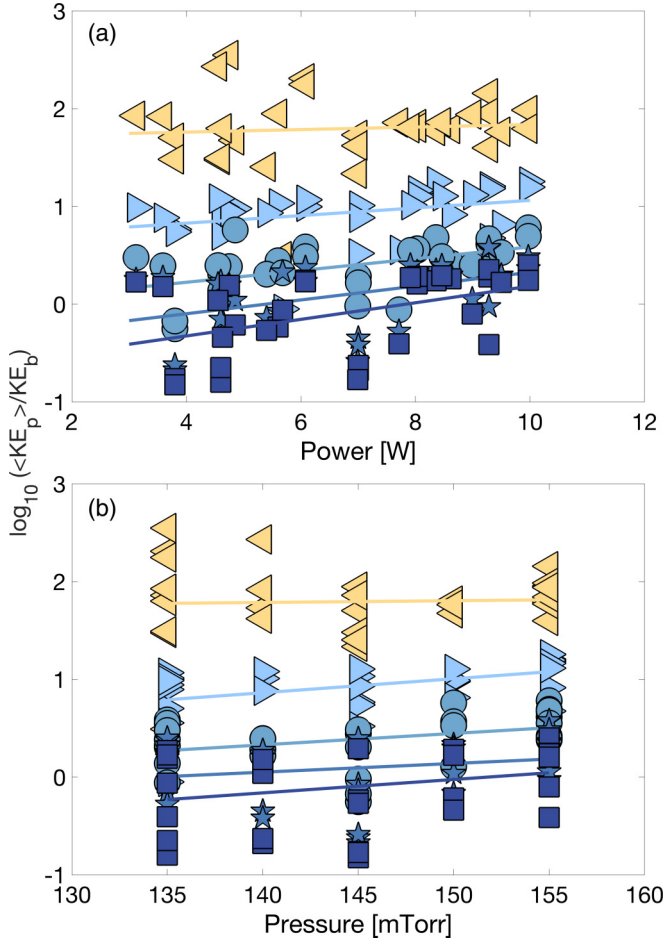
FIG. 12. The average kinetic kinetic energy of torsion particle as a function of (a) power and (b) pressure. From the top down, left-pointing triangles denote the data for torsion particles, right-pointing triangles for cage particles, circles for second-shell particles, stars for third-shell particles, and squares for background particles. Trend lines correspond to data points of the same shell.
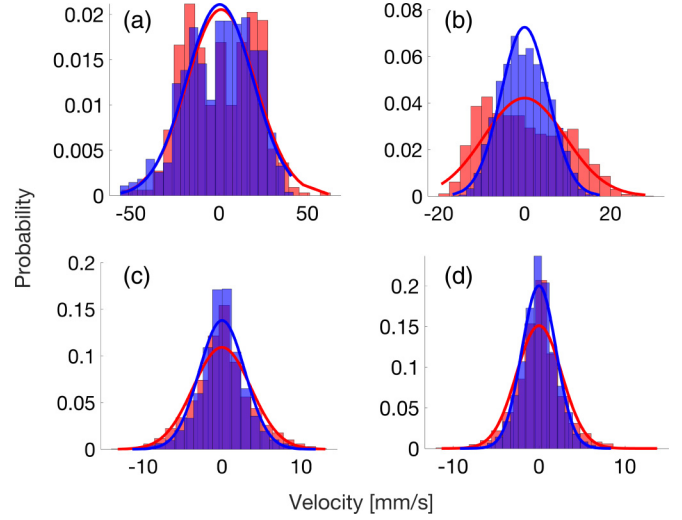

FIG. 13. The velocity distributions of the torsion particles (a), cage particles (b), particles in the second shell (c), and particles in the third shell (d). Red bars indicate x velocities, and blue bars indicate y velocities. The red lines are Maxwellian distributions for x velocities, and the blue lines are for the y velocities.

the local area (i.e., two to three shells) for the pressure and power range examined.

When no torsion is present, the average background kinetic energy ranges from $KE_b = 0.16$–0.51 eV. Across the same experimental parameter space, the kinetic energy of background particles with a torsion in the lattice ranges between $KE_b = 0.13$–1.04 eV. A single torsion increases the kinetic energy of the leader and satellite particles to $KE_{pT} = 25.96$–86.58 eV with the average $\langle KE_p \rangle = 57.76$ eV. The increase in kinetic energy observed in the paired particles is due to the repetitive circular motion of the torsion. At the same time, the kinetic energy of cage particles increases to $KE_{pC} = 3.25$–19.47 eV with $\langle KE_{pC} \rangle = 9.86$ eV. The kinetic energy of the second and third shell particles increases to $KE_{p2} = 1.17$–5.71 eV and $KE_{p3} = 0.65$–2.47 eV, respectively, with averages of $\langle KE_{p3} \rangle = 2.86$ eV and $\langle KE_{p3} \rangle = 1.60$ eV. Particles at the fourth shell and beyond had similar kinetic energy to the background, $KE_{p4} = KE_b$ as shown in Fig. 11. The average kinetic energy for the particles as a function of power and pressure are shown in Fig. 12. The kinetic energy measurements may

not detect this increase in anisotropy of particle motion as the particles move at the same average velocity.

In Fig. 13, we show the particle velocity distribution for the various types of particles. The velocities of the particles in this figure are rotated such that the x axis is directed along the radial direction, pointing away from the torsion equilibrium position (negative values indicate velocities pointed towards the torsion particles). The y velocities are perpendicular to this direction. The torsion particles do not have a Maxwellian distribution, which is attributable to their constant-driven circular to elliptical motion. The cage particles have non-Maxwellian velocity distributions in the x direction, while the y velocity distribution is Maxwellian. The distribution is skewed towards negative x velocities, consistent with the wakefield attraction of the leader particle being weaker than the repulsion by the satellite. The second and third shell particles tend toward Maxwellian distributions, with the second shell particles displaying larger velocities than the third shell, which is expected for shells closer to the torsion particles. The second and third shells also have different kinetic energies in the rotated coordinate system's x and y directions, with greater kinetic energy in the radial x direction.

B. Radial amplitude

A measurement of a particle's displacement from its equilibrium position is used to quantify the greatest "reach" of the torsion. The radial amplitude is the maximum distance a particle travels from its equilibrium position compared to the average displacement, as shown in Fig. 14. This diagnostic method yields a higher resolution for the torsion's effect on the motion of particles further from the torsion compared to the average kinetic energy as shown in Fig. 11. The increase in maximum amplitude is related to the variance in the particle motion increasing even while maintaining the same average displacement and velocity. Figure 14 provides a pseudo heat
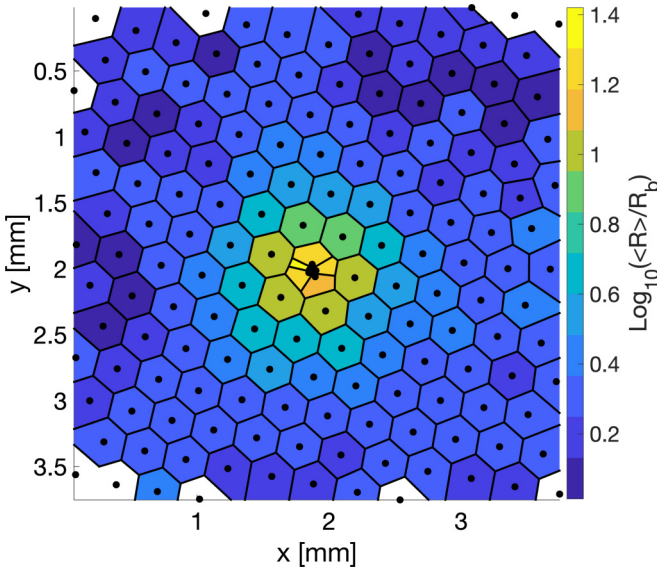
FIG. 14. Radial amplitude of particle motion. The measurements are normalized by their background values, R_b. Operating parameters were 145 mTorr and 4.75 W.
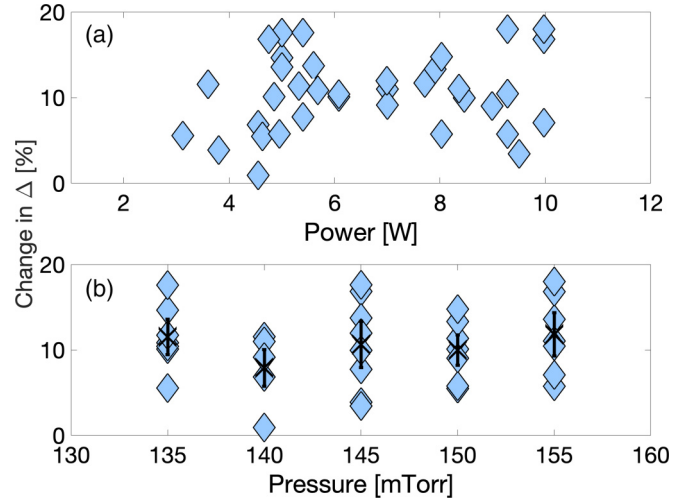

FIG. 15. The percent change in interparticle spacing with a torsion present as a function of (a) power and (b) pressure. Diamonds are the result of individual crystals with torsions. The crosses in (b) are the mean of each set with standard deviation at a given pressure indicated by the error bars.

map for a torsion and the surrounding crystal area, with the hottest areas showing a large amplitude of motion away from the microparticle equilibrium position and the colder areas indicating that the particle remains near its equilibrium point. Over the parameter space studied, both the leader and satellite particles exhibit a radial amplitude 10.5 ± 4.1 times that of the background particles, with the cage particles showing an average amplitude of 4.2 ± 1.3 times the background measurement of the radial amplitude. However, even particles far from the torsion have a maximum displacement of 2.2 ± 0.4 times that of the background particles. This reveals that the energy from the torsion is transmitted over the whole crystal, as the radial amplitude for each particle doesn't return to the background value.

C. Crystalline structure

Crystalline structure can be characterized by pair correlation functions, which describe interparticle spacings, Voronoi diagrams, which indicate hexagonal symmetry; and angular correlation functions (i.e., bond order), which show the short- and long-range order of the plasma crystal [4,11,36,40–49].

Pair correlation functions, PCFs, are routinely used to identify the phase of the system (solid, liquid, gas). Examining the PCF for a sample crystal with and without a torsion shows that a torsion increases the interparticle spacing by 11% (Fig. 7) throughout the crystal. The far-reaching structure of the PCF at $|r| > 1$ mm becomes less sharp; at $|r| > 1.3$ mm, there is a noticeable loss in order as the peaks disappear completely, indicating a loss in long-range order.

Figure 15 displays the increase in average interparticle spacing for all the crystals with torsions as a function of power and pressure. The increase in interparticle spacing is relatively constant across both the range of powers and pressures investigated; we surmise that the increase in interparticle spacing is strictly due to the torsion present in the lattice. Increases in interparticle spacing allow for more freedom of movement for

the microparticles surrounding the torsion particles; however, particles do not move at faster speeds with the increased range of motion as the average kinetic energy remains much the same.

The hexagonal symmetry of a crystal is measured by the bond order correlation function,

$$|\psi_6| = \left| \frac{1}{M} \sum_{m=1}^{M} e^{6i\Theta_{jm}} \right| \qquad (3)$$

where M is the number of particles and Θ is the angle between particle j and particle m. For a crystal with perfect hexagonal order, the value of $|\psi_6|_j$ in each cell centered on particle j equals one. A decrease in the values of $|\psi_6|_j$ then signals a decrease in the hexagonal order of the lattice site. In the sample crystal shown in Fig. 16, the average value of the bond order parameter, $|\psi_6|$, is 0.66 for the cage particles, 0.9 within the first shell and then approaches one at the third shell; this indicates major structural disruption occurs locally (within two to three shells) before the system relaxes to a crystalline structure. Crystals in this study contained hundreds to thousands of particles, and the torsion disturbance is relatively small. Multiple torsions would be needed to significantly change the lattice symmetry on a systemic scale.

V. CONCLUSIONS

The effects of a single torsion on the surrounding particles and its short-range structural effects on the crystalline lattice have been detailed. A single torsion results in an increased radial amplitude of motion and an asymmetry in the particle velocity distributions for all particles in the crystal, resulting in a "hot crystal." Locally, the motion of the cage, second, and third-shell particles in the crystal plane, and vertical motion outside the monolayer, are increased significantly compared to the motion of particles in crystals without torsions. Surprisingly, a single torsion also increases the variance in the
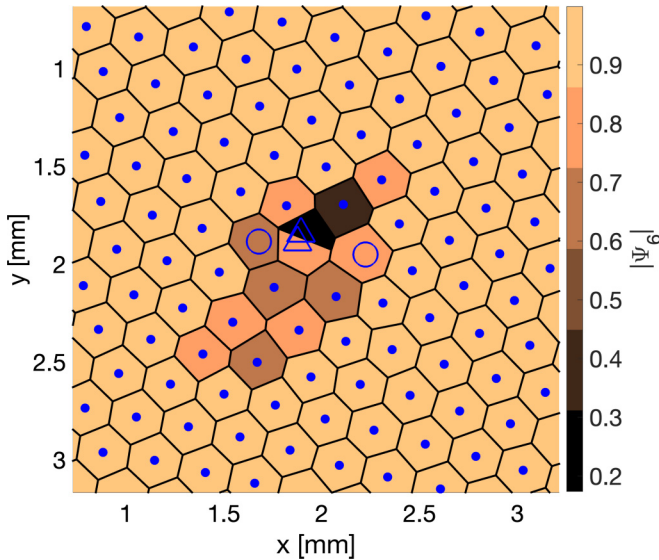
FIG. 16. The hexagonal symmetry of the crystal surrounding a torsion for a single frame. The color of the cells in the Voronoi diagram indicates the bond order parameter. Closed circles indicate the particle positions, open circles denote particles with sided-sided cells, closed circles are six-sided cells, and triangles are five-sided cells. In this frame, the leader and satellite particles are the two triangles sharing a cell. Operating conditions 150 mTorr and 4.9 W.

particle motion for all particles even when the average KE remains the same. The increased variance in motion of the microparticles observed far from the torsion indicates that the torsion creates systemic changes on a larger scale than previously noted in other torsion experiments.

Particles that move at the same speed as background particles but have a larger variance in their motion are likely due to the increased spacing in the crystal and the elliptical motion of the cage particles, allowing a greater range of motion along the direction of the cage particle motion. The torsion "reach"

determined through the average radial amplitude surpasses the torsion "reach" obtained through kinetic energy measurements. The increase in kinetic energy is observed in two to three shells outside of the torsion, while the increase in radial amplitude is observed throughout the crystal. A torsion pair within a lattice transforms the system into a "hot crystal" not just because of the local increase in KE_p, but also because the variance in particle position increases.

Structurally, including a single torsion increases the interparticle spacing within the crystal by an average of 11%. Increased spacing in the lattice can aid in the production of more torsions. The increase in interparticle spacing due to a torsion is similar to that seen in a crystal subjected to a sharp drop in pressure as reported in Refs. [25,26]. Therefore, more torsions may be easily formed once a single torsion is in the lattice. A decrease in far-range order measured by $g(r)$ was observed for $r > 1.3$ mm; however, the hexagonal symmetry measured by the bond angle correlation parameter shows that the decrease in crystal symmetry extends only to the cage and second-shell particles.

The above findings confirm that when a torsion is present in a plasma crystal lattice, constants that govern motion in the lattice (interparticle spacing, hexagonal symmetry, motion) are altered locally. Kinetic energy increases by a factor of two to three, and the loss of far-range order leads to a fundamentally different system than a crystal without a torsion. The increase in kinetic energy for the local torsion particles, long-range structural changes in the lattice, and the absence of melting strongly indicate that crystals with a torsion included can be considered hot crystals. Future work will look at the interaction of torsions with each other and their role in two-dimensional phase transitions.

[1] A. Melzer, *Physics of Dusty Plasmas: An Introduction*, Lecture Notes in Physics, Vol. 962 (Springer International Publishing, Cham, 2019).

[2] G. E. Morfill and A. V. Ivlev, Complex plasmas: An interdisciplinary research field, Rev. Mod. Phys. **81**, 1353 (2009).

[3] A. Piel, *Plasma Physics* (Springer, Berlin, 2010).

[4] H. Thomas, G. E. Morfill, V. Demmel, J. Goree, B. Feuerbacher, and D. Möhlmann, Plasma crystal: Coulomb crystallization in a dusty plasma, Phys. Rev. Lett. **73**, 652 (1994).

[5] J. Goree, D. Samsonov, Z. W. Ma, A. Bhattacharjee, H. M. Thomas, U. Konopka, and G. E. Morfill, Monolayer plasma crystals, *Frontiers in Dusty Plasmas* (Elsevier, Amsterdam, 2000), pp. 91–97.

[6] A. Melzer, V. A. Schweigert, I. V. Schweigert, A. Homann, S. Peters, and A. Piel, Structure and stability of the plasma crystal, Phys. Rev. E **54**, R46 (1996).

[7] H. Ikezi, Coulomb solid of small particles in plasmas, Phys. Fluids **29**, 1764 (1986).

[8] V. Nosenko, J. Goree, Z. W. Ma, and A. Piel, Observation of shear-wave Mach cones in a 2D dusty-plasma crystal, Phys. Rev. Lett. **88**, 135001 (2002).

[9] A. Melzer, S. Nunomura, D. Samsonov, Z. W. Ma, and J. Goree, Laser-excited Mach cones in a dusty plasma crystal, Phys. Rev. E **62**, 4162 (2000).

[10] J. Kong, K. Qiao, L. S. Matthews, and T. W. Hyde, Temperature measurement of a dust particle in a RF plasma GEC reference cell, J. Plasma Phys. **82**, 905820505 (2016).

[11] M. G. Hariprasad, P. Bandyopadhyay, G. Arora, and A. Sen, Experimental observation of a first-order phase transition in a complex plasma monolayer crystal, Phys. Rev. E **101**, 043209 (2020).

[12] K. J. Strandburg, Two-dimensional melting, Rev. Mod. Phys. **60**, 161 (1988).

[13] K. Takahashi, Y. Hayashi, and K. Tachibana, Two-dimensional melting in a Coulomb crystal of dusty plasmas, Jpn. J. Appl. Phys. **38**, 4561 (1999).

[14] L. S. Matthews, D. L. Sanford, E. G. Kostadinova, K. S. Ashrafi, E. Guay, and T. W. Hyde, Dust charging in dynamic ion wakes, Phys. Plasmas **27**, 023703 (2020).

[15] R. Kompaneets, G. E. Morfill, and A. V. Ivlev, Wakes in complex plasmas: A self-consistent kinetic theory, Phys. Rev. E **93**, 063201 (2016).

[16] I. H. Hutchinson, Intergrain forces in low-Mach-number plasma wakes, Phys. Rev. E **85**, 066409 (2012).

[17] W. J. Miloch, Numerical simulations of dust charging and wake-field effects, J. Plasma Phys. **80**, 795 (2014).

[18] A. Melzer, Connecting the wakefield instabilities in dusty plasmas, Phys. Rev. E **90**, 053103 (2014).

[19] A. V. Ivlev, J. Bartnick, M. Heinen, C.-R. Du, V. Nosenko, and H. Löwen, Statistical mechanics where Newton's third law is broken, Phys. Rev. X **5**, 011035 (2015).

[20] V. A. Schweigert, I. V. Schweigert, V. Nosenko, and J. Goree, Acceleration and orbits of charged particles beneath a monolayer plasma crystal, Phys. Plasmas **9**, 4465 (2002).

[21] C.-R. Du, V. Nosenko, S. Zhdanov, H. M. Thomas, and G. E. Morfill, Interaction of two-dimensional plasma crystals with upstream charged particles, Europhys. Lett. **99**, 55001 (2012).

[22] K. Takahashi, Y. Hayashi, S. Nishino, and K. Tachibana, Analyses of attractive forces between particles in laboratory dusty plasmas, Phys. Scr. **T89**, 37 (2001).

[23] K. T. K. Takahashi, T. O. T. Oishi, K.-i. S. K.-i. Shimomai, Y. H. Y. Hayashi, and S. N. S. Nishino, Simple hexagonal Coulomb crystal near a deformed plasma sheath boundary in a dusty plasma, Jpn. J. Appl. Phys. **37**, 6609 (1998).

[24] S. K. Zhdanov, L. Couëdel, V. Nosenko, H. M. Thomas, and G. E. Morfill, Spontaneous pairing and cooperative movements of micro-particles in a two dimensional plasma crystal, Phys. Plasmas **22**, 053703 (2015).

[25] V. Nosenko, S. K. Zhdanov, H. M. Thomas, J. Carmona-Reyes, and T. W. Hyde, Dynamics of spinning particle pairs in a single-layer complex plasma crystal, Phys. Rev. E **96**, 011201(R) (2017).

[26] V. Nosenko, S. K. Zhdanov, H. M. Thomas, J. Carmona-Reyes, and T. W. Hyde, Spontaneous formation and spin of particle pairs in a single-layer complex plasma crystal, Europhys. Lett. **112**, 45003 (2015).

[27] T. W. Hyde, J. Kong, and L. S. Matthews, Helical structures in vertically aligned dust particle chains in a complex plasma, Phys. Rev. E **87**, 053106 (2013).

[28] V. Land, E. Shen, B. Smith, L. Matthews, and T. Hyde, Experimental and computational characterization of a modified GEC cell for dusty plasmaexperiments, New J. Phys. **11**, 063024 (2009).

[29] See Supplemental Material at http://link.aps.org/supplemental/10.1103/PhysRevE.110.025205 for top and side torsion videos (25 and 10 FPS) are provided with corresponding tracking data (tracks of particles are shown in different colors).

[30] M. G. Hariprasad, P. Bandyopadhyay, V. S. Nikolaev, D. A. Kolotinskii, S. Arumugam, G. Arora, S. Singh, A. Sen, and A. V. Timofeev, Self-sustainednon-equilibrium co-existence of

[31] fluid and solid states in a strongly coupled complex plasma system, Sci. Rep. **12**, 13882 (2022).

[31] B. Liu, J. Goree, and Y. Feng, Non-Gaussian statistics and superdiffusion in a driven-dissipative dusty plasma, Phys. Rev. E **78**, 046403 (2008).

[32] C. Schmidt and A. Piel, Stochastic heating of a single Brownian particle by charge fluctuations in a radio-frequency produced plasma sheath, Phys. Rev. E **92**, 043106 (2015).

[33] V. A. Schweigert, I. V. Schweigert, A. Melzer, A. Homann, and A. Piel, Plasma crystal melting: A nonequilibrium phase transition, Phys. Rev. Lett. **80**, 5345 (1998).

[34] R. Ichiki, Y. Ivanov, M. Wolter, Y. Kawai, and A. Melzer, Melting and heating of two-dimensional Coulomb clusters in dusty plasmas, Phys. Rev. E **70**, 066404 (2004).

[35] Y. Ivanov and A. Melzer, Melting dynamics of finite clusters in dusty plasmas, Phys. Plasmas **12**, 072110 (2005).

[36] W. D. S. Ruhunusiri, J. Goree, Y. Feng, and B. Liu, Polygon construction to investigate melting in two-dimensional strongly coupled dusty plasma, Phys. Rev. E **83**, 066402 (2011).

[37] H. Totsuji, Structure and melting of two-dimensional dust crystals, Phys. Plasmas **8**, 1856 (2001).

[38] L. Couëdel, S. K. Zhdanov, A. V. Ivlev, V. Nosenko, H. M. Thomas, and G. E. Morfill, Wave mode coupling due to plasma wakes in two-dimensional plasma crystals: In-depth view, Phys. Plasmas **18**, 083707 (2011).

[39] V. Steinberg, R. Sütterlin, A. V. Ivlev, and G. Morfill, Vertical pairing of identical particles suspended in the plasma sheath, Phys. Rev. Lett. **86**, 4540 (2001).

[40] V. Nosenko, S. K. Zhdanov, A. V. Ivlev, C. A. Knapek, and G. E. Morfill, 2D melting of plasma crystals: Equilibrium and nonequilibrium regimes, Phys. Rev. Lett. **103**, 015001 (2009).

[41] A. V. Zampetaki, H. Huang, C.-R. Du, H. Löwen, and A. V. Ivlev, Buckling of two-dimensional plasma crystals with non-reciprocal interactions, Phys. Rev. E **102**, 043204 (2020).

[42] B. Smith, J. Vasut, T. Hyde, L. Matthews, J. Reay, M. Cook, and J. Schmoke, Dusty plasma correlation function experiment, Adv. Space Res. **34**, 2379 (2004).

[43] M. G. Hariprasad, P. Bandyopadhyay, G. Arora, and A. Sen, Experimental investigation of test particle induced microstructural changes in a finite two-dimensional complex plasma crystal, Phys. Plasmas **26**, 103701 (2019).

[44] A. Melzer, A. Homann, and A. Piel, Experimental investigation of the melting transition of the plasma crystal, Phys. Rev. E **53**, 2757 (1996).

[45] J. B. Pieper, J. Goree, and R. A. Quinn, Experimental studies of two-dimensional and three-dimensional structure in a crystallized dusty plasma, J. Vac. Sci. Technol. A **14**, 519 (1996).

[46] S. O. Yurchenko, N. P. Kryuchkov, and A. VIvlev, Interpolation method for pair correlations in classical crystals, J. Phys.: Condens. Matter **28**, 235401 (2016).

[47] E. V. Vasilieva, O. F. Petrov, and M. M. Vasiliev, Laser-induced melting of two-dimensional dusty plasma system in RF discharge, Sci. Rep. **11**, 523 (2021).

[48] Y. Feng, B. Liu, and J. Goree, Rapid heating and cooling in two-dimensional Yukawa systems, Phys. Rev. E **78**, 026415 (2008).

[49] M. Zuzic, A. V. Ivlev, J. Goree, G. E. Morfill, H. M. Thomas, H. Rothermel, U. Konopka, R. Sütterlin, and D. D. Goldbeck, Three-dimensional strongly coupled plasma crystal under gravity conditions, Phys. Rev. Lett. **85**, 4064 (2000).